Project Title: Global Distribution of Carbonyl Sulphide with IASI

Supervisor: Dr Anu Dudhia

Name: Edwin Phua

Abstract. Remote sensing via satellite infrared sounding enables measurement of trace gas distributions on a global scale. The global distribution of carbonyl sulphide (OCS) is found using the Scaled Linear Retrieval (SLR) on spectral data from the Infrared Atmospheric Sounding Interferometer. The results indicate that the global distribution is dominated by primary oceanic sources and vegetative sinks. However, unexpected amplification of signals at night and in hemispheric winters were observed over land surfaces. High retrieved values were also observed in desert regions without any known sources. Investigation of the SLR showed that diurnal variation and anomalously high values in sandy deserts are likely due to interference from surface spectral emissivity features and diurnal emissivity variation. Improvements to the SLR were proposed, namely in expanding the range of atmospheric profiles used and in accounting for variable surface emissivity.

1. INTRODUCTION

Carbonyl sulphide (OCS) is the longest-lived and most abundant sulphur species in the atmosphere [1, 2]. It has a largely uniform global distribution, residing mostly in the troposphere with an average mixing ratio of ~500 parts per trillion volume and a residence lifetime of ~2–6 years [2, 3]. OCS abundance and its long lifetime are due to both its global source terms and its relative inertness to tropospheric chemistry. In comparison, other emitted sulphur species (sulphur dioxide (SO_2), dimethyl sulphide (DMS), hydrogen sulphide (H_2S) and carbon disulphide (CS_2)) have much shorter tropospheric lifetimes (~days) and lower overall abundances, due to rapid oxidation and removal from the troposphere by wet and dry deposition [4, 5].

OCS is a critical component of the global sulphur cycle [6, 7]. Due to its tropospheric abundance and lifetime, OCS is the primary contributor to the stratospheric sulphur budget and aerosol loading in volcanically quiescent periods [1, 8]. This has global warming implications, since OCS exerts negative radiative forcing through its contribution to the aerosol layer, yet itself exerts positive forcing as a greenhouse gas [1].

OCS is also involved in key carbon cycle processes [9, 6]. In particular, OCS and CO_2 are consumed by plant enzymes involved in photosynthesis. This results in correlated plant uptakes of OCS and CO_2, which has motivated research into using OCS as a proxy for photosynthetic carbon uptake and gross primary production [6]. It has the added advantage of not having major co-located sources and sinks, unlike CO_2, which make carbon-uptake by OCS easier to gauge [6, 9].

OCS has infrared absorption features, which allows it to be remotely measured by satellite infrared soundings. For this project, data was taken from the Infrared Atmospheric Sounding Interferometer (IASI), and column amounts of OCS were retrieved using the new experimental Scaled Linear Retrieval (SLR) [10]. The aim of this project is to analyse the global OCS distribution, to evaluate known and predicted spatiotemporal trends from previous results and literature, and to appraise the performance of the SLR.

2. BACKGROUND

In this section, the major and minor sources and sinks of OCS are described, and previous instances of satellite OCS measurement are briefly discussed.

2.1 Sources

Sources in the global OCS budget are widely accepted to be dominated by oceans (~50–80%), with the remainder attributed mainly to anthropogenic activity and other natural sources [9, 11]. The size of the ocean source is disputed; studies that gave higher estimates attributed additional source terms to the ocean in order to balance a sink-heavy top-down budget [7, 9, 12]. Recent bottom-up estimates, however, assign more conservative figures to the ocean source. Instead, larger contributions are attributed to anthropogenic activities previously unaccounted for, notably from industrial processes in China [6, 13, 14].

OCS emissions from oceans and coastal areas occur via direct and indirect processes [1, 12, 9]. Indirect production takes place through oxidation of other sulphur gases emitted from the ocean, and is estimated to form the majority (~60–80%) of oceanic production [1, 3, 9]. The most common precursors are DMS and CS_2. CS_2 is generated by photochemical reactions in seawater, whereas DMS is produced biologically in certain classes of marine phytoplankton [15, 7]. DMS emission is regarded as a significant source of OCS [1, 16]. Moreover, recent findings from better laboratory-based atmospheric simulations have found evidence for an alternate DMS degradation pathway in the atmosphere [17]. This could lead to higher yield of DMS-to-OCS than previously assumed, and consequently greater DMS contribution to global OCS.

OCS is also directly produced in seawater from reactions involving dissolved organic matter (DOM).

This occurs via photochemical and thermal pathways in the sunlit uppermost ocean layer (photic zone). Direct emissions form a smaller fraction of the ocean source due to low OCS production rates and its rapid hydrolysis in seawater [18].

Anthropogenic OCS emissions occur through a variety of industrial processes. Some of these generate OCS directly, though the majority of production occurs via oxidation of other sulphur gases like CS_2 [6, 11]. OCS is also produced from biomass burning, which mainly occurs in forested regions in the tropics with large inter-annual and seasonal variation [19]. Altogether, these are estimated to comprise 20–50% of global production.

Other minor natural sources include anoxic soils in wetlands. Precipitation was also found to produce OCS via photochemical reactions, though there is a notable lack of further research into this phenomenon [1, 20]. Volcanic activity is also a minor source, making up less than 1% of global emissions [21].

2.2 Sinks

The terrestrial biosphere is a well-known primary sink, constituting the bulk (~75–95%) of global consumption in all budget estimates considered [1, 3, 6, 7, 9, 12]. Recent systematic reviews present bottom-up estimates which attribute most of this terrestrial uptake to vegetation (~80–90%), and the rest to oxic soils [6].

Plant OCS removal pathways are well known; OCS is taken up by plant stoma and irreversibly hydrolysed by enzymes involved in photosynthesis [6, 22]. This leads to correlated uptakes of OCS with photosynthetic activity, which is supported by ecosystem flux measurements in temperate forested regions [22]. Previous literature has also found significant overall night time contributions (~30%) to total OCS uptake by plants, arising from incomplete night time stomatal closure and light-independence of enzyme activity [22, 23]. OCS uptake by oxic soils has been measured and linked to a variety of environmental factors, but the exact mechanisms remain unknown [22, 6].

The remainder of the budget (~10–20%) is attributed to secondary atmospheric sinks. Slow OCS removal in the free troposphere occurs mostly through oxidation by hydroxyl radicals (OH) [7, 24, 9, 6]. Due to its tropospheric inertness and long lifetime, OCS is also removed by slow transport into the stratosphere [1, 2]. It then undergoes ultraviolet photolysis or reactions with oxygen atoms, and reacts further to eventually contribute to the stratospheric aerosol layer [2].

2.3 Previous satellite measurements

Over the past 2 decades, various satellite measurements of global tropospheric OCS distributions have been performed [6]. Glatthor et al. (2015) reported on global OCS features identified by the Michelson Interferometer for Passive Atmospheric Sounding (MIPAS) [12]. The results from a dataset spanning 2002 to 2012 exhibited two main features: enhanced amounts over the Pacific, and seasonal depletion over tropical South America to Africa. These provide evidence for the major oceanic source and vegetative sink. However, as a limb-viewing instrument, MIPAS has poor longitudinal spatial resolution, and a limited vertical coverage which penetrates to the upper troposphere at its deepest.

Nadir-viewing measurements of OCS were published by Kuai et al. (2015) using data from the Tropospheric Emission Spectrometer (TES) [25]. However, retrievals with TES are limited to oceans at latitudes <40˚. This was due to poor signal-to-noise ratio from low thermal contrast at higher latitudes, and surface spectral emissivity (SSE) complexities over land.

Vincent and Dudhia (2017) reported on work with IASI [26], which performs nadir measurements like TES but with better spatial coverage. Global distributions from previous IASI retrievals had similar features to those identified from MIPAS data. Higher IASI resolution compared to TES and MIPAS also revealed previously unobserved features, such as OCS depletion over the Intertropical Convergence Zone (ITCZ) [6].

The results from previous satellite measurements form an added basis of comparison and evaluation of OCS patterns and the performance of the new SLR algorithm.

3. METHODS

3.1 Infrared Atmospheric Sounding Interferometer

Spectral data for this project was taken from IASI, which is the nadir-viewing Fourier Transform interferometer aboard the European MetOp satellites [27]. The satellites follow a sun-synchronous orbit, crossing the equator from north to south and vice versa at local times of 09:30 and 21:30 respectively. Near-global day and night coverage in 24 hours is achieved due to wider spatial coverage from scanning transverse to the orbital path. The ground pixel size for IASI

observations is 12 km × 12 km. IASI records infrared atmospheric emissions in the wavenumber region of 645 cm^{-1} and 2760 cm^{-1}, with a spectral resolution of 0.5 cm^{-1} after apodisation[1]. IASI spectral data is used to obtain atmospheric temperature and water vapour profiles for weather forecasting. Atmospheric column amounts of various molecules are also retrieved from spectral data using their unique spectral signatures.

OCS infrared absorption is characterized by strong peaks between 2040 cm^{-1} and 2080 cm^{-1} (Fig. 1). However, the size of the absorption feature alone is insufficient to determine the column amount of an absorber. First, interference due to absorption by other molecules (Fig. 1) must be accounted for. Secondly, infrared soundings measure absorption features based on the thermal contrast between the warmer surface of the earth and the cooler atmosphere containing the molecule. This makes soundings more sensitive to molecule concentrations at the colder higher altitudes as opposed to near the surface due to larger surface-atmosphere temperature differences. For IASI, peak OCS sensitivity was found consistently at ~500 hPa, around the mid-troposphere [26]. As a consequence, the size of the absorption feature is influenced by column amount, thermal contrast with the surface and the vertical distribution of the absorber.

3.2 Scaled Linear Retrieval (SLR)

The SLR is a new, experimental 'fast' retrieval algorithm developed in AOPP, intended to retrieve the concentrations of a large number of trace gases with minimal computational time [10]. It generates the total column amounts of OCS from IASI spectra between 2000 cm^{-1} to 2100 cm^{-1}. An ensemble of reference atmospheric profiles (~100s) is used to account for background atmospheric features to isolate the OCS signature. The profiles are generated by a radiative transfer model called the Reference Forward Model (RFM) [28], using meteorological data from a spread of locations. Additional profiles were generated by varying near surface temperatures by ±10 K.

A Singular Vector Decomposition (SVD) is performed on the ensemble of profiles to identify its main spectral patterns. These patterns are meant to account for absorption and variability of other molecules in the atmosphere. A simultaneous fit is performed on IASI spectral data using these spectral patterns and the OCS

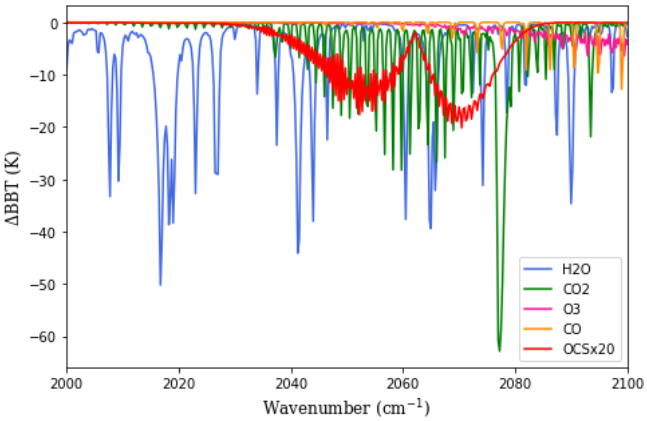

Figure 1: Change in brightness temperatures due to a typical atmospheric mixture of gases which absorb strongly between 2000 cm^{-1} to 2100 cm^{-1}. The OCS signature is characterized by two strong peaks, enhanced ×20 in the plot for clearer visualization. Signals were generated using the RFM.

spectral signature to yield the OCS column amount. To further account for factors such as poor thermal contrast over colder regions, a scale-factor is similarly retrieved and applied to the column amount.

3.3 Data processing

Retrieved column amounts were filtered for quality. Values with a cloud fraction of >50% were omitted due to large interference from cloud water absorption in the infrared. Data with satellite zenith angles >40˚ were filtered out to avoid interference arising from angular behaviour of infrared SSE. This behaviour has been observed at angles >40˚ for quartz in sandy desert areas [29] and for ocean surfaces [30]. Erroneous values flagged by the SLR were also filtered out.

After filtering, OCS column values were separated into seasonal quarter-yearly intervals[2] from December 2017 to November 2018, to observe seasonal patterns within the year. Day and night values were separated to reveal any diurnal variation in retrieved values.

Values were sorted into 0.5˚ × 0.5˚ latitude-longitude bins. The median value for each bin was chosen to reduce sensitivity to extreme outliers. In the case of the retrieval, low thermal contrasts could generate exceptionally high or low column amounts due to noise, which would artificially skew the mean.

On average, around 100 filtered pixel values are processed per bin in each plot. Ground sizes of the lat-lon bins are typically larger than the pixel size, except at very high latitudes (>75˚) where the east-west bin length becomes comparable to pixel size. In order to reduce errors due to anomalous cases, only bins with >10 pixels are shown.

[1] Wavenumbers are the reciprocal of wavelengths, denoted in units [cm^{-1}].
[2] Quarter-yearly intervals and corresponding boreal seasons: Dec to Feb (DJF) - Winter, Mar to May (MAM) - Spring, Jun to Aug (JJA) - Summer, Sep to Nov (SON) - Fall

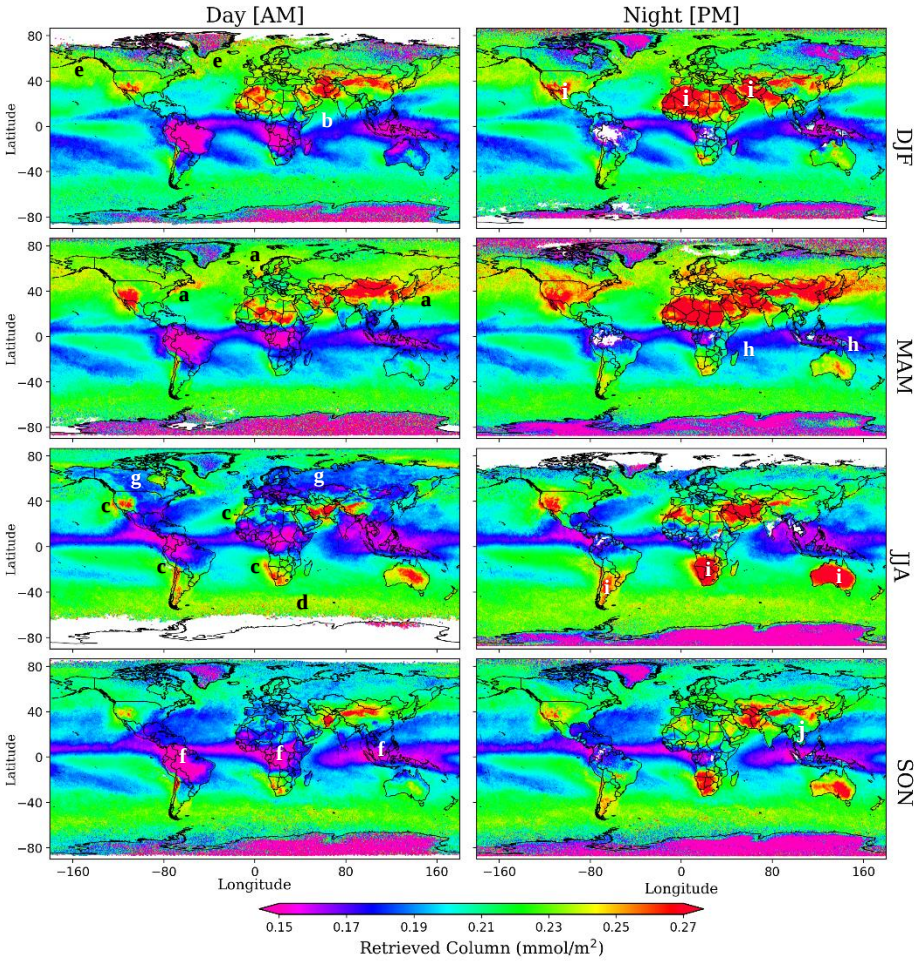

Figure 2: Day (left column) and night (right column) median retrieved OCS column amounts in 0.5˚×0.5˚ latitude-longitude boxes, in quarter-yearly intervals of DJF (top row), MAM (second row), JJA (third row) and SON (bottom row), for end 2017 to 2018. Regions without data are represented in white. Lettering are labels for regions highlighted in the discussions of the results.

4. RESULTS & DISCUSSION

The global day and night distributions for each quarter-yearly seasonal interval are shown (Fig. 2). Observations related to the oceanic sources and vegetative sinks are explored first. Diurnal and seasonal variation is discussed next, and finally certain anomalies are considered.

4.1 Oceanic source

Significant sources of OCS are expected to be spatially correlated with features of relatively high OCS levels in the global distribution. These features should also reflect the seasonal variability of the source terms.

Two chief modes of oceanic production are considered. The first is via photochemical pathways involving DOM, which is remotely measured using chromophoric DOM (CDOM) as its proxy. CDOM is the pigmented component of DOM, and its quantities in the photic zone can be derived from visible ocean colour measurements by satellites. The second mode is through oxidation of DMS produced by phytoplankton. Chlorophyll-*a* (CHLA) amounts serve as the proxy for phytoplankton quantities, since like CDOM it can be remotely measured using visible ocean colour [31].

Global distributions of CDOM and CHLA are compared with the results for OCS. Aurin et al. (2018) presents the 12-year averaged seasonal distributions of CDOM and CHLA–CDOM measured by the Moderate Resolution Imaging Spectroradiometer (MODIS) from 2002 to 2014 (Fig. 3) [32]. CHLA–CDOM refers to the difference in CHLA and CDOM amounts. From Fig. 3, both these distributions have similar spatial and seasonal trends, though CHLA has larger variation. A significant seasonal CHLA and CDOM difference is apparent in the North Atlantic for boreal winter.

Comparisons of the results for OCS with CDOM and CHLA distributions reveal several possibly correlated features. Seasonal increase in northern hemispheric CHLA and CDOM amounts during boreal spring coincide with stronger OCS signatures. This is notably observed in the northwest Atlantic, the Baltic and Norwegian seas, the northwest Pacific and the Sea of

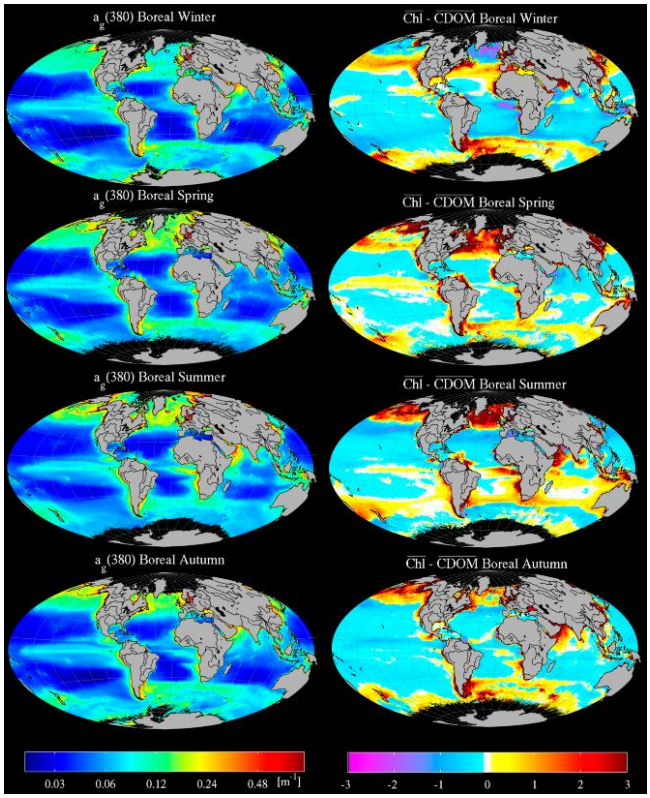

*Figure 3: 12-year averaged CDOM (left) and CHLA-CDOM (right) quarter-yearly distributions from MODIS data (Aurin et al., Appl. Sci., **8**(12) 2687 (2018)).*

Japan (Fig. 2, MAM, points 'a'). CHLA abundance and relatively high OCS are also observed in the northwest Arabian sea for most of the year (Fig. 2, DJF, 'b').

OCS production has been observed in well-known biologically active regions of upwelling nutrient rich waters [26]. Upwelling exposes deep ocean DOM to sunlight by transport into the photic zone, and also carry nutrients which provide thriving conditions for phytoplankton. Prominent examples are the Eastern Boundary Current Systems (EBCS), comprising the California and Humboldt current systems in the Pacific, and the Canary and Benguela currents in the Atlantic [33]. Ekman transport induces coastal upwelling in these regions, which leads to high biological activity. Another example is the biologically productive Southern Sub-Tropical Front (SSTF), where the cold Antarctic Circumpolar Current (ACC) mixes with warmer sub-Antarctic waters [34].

From the results (Fig. 2), relatively high OCS levels are consistently observed all-year-round in the four EBCS regions (Fig. 2, JJA, 'c'). This is similarly the case over the SSTF (Fig. 2, JJA, 'd'). The spatial correlation with these biologically active regions thus support oceanic DOM and phytoplankton as sources, and corroborate with previous results obtained from IASI [26].

The features over the EBCS regions in Fig. 2 also exhibit south/north-westward transport towards the equator that is not observed in Fig. 3. Note that distributions of CHLA and CDOM are in the ocean, while IASI measures OCS in the atmosphere. As a consequence, the global OCS distribution is expected to be further modified by prevailing tropospheric winds, especially because of its long residence lifetime. Convective Hadley cells generate north/south easterly trade winds in the northern/southern hemispheres, which begin at mid latitudes and converge at the ITCZ. These wind patterns match well with the observed EBCS features, which further validate the EBCS source.

However, despite the general correlations between OCS and CDOM/CHLA features, there are some key discrepancies. Notably, both phytoplankton DMS production and photochemical DOM pathways are light dependent processes [6, 35]. As a consequence, OCS abundances are expected to follow seasonal light availability. However, an inverse relationship is found, with a peak in the hemispheric winter and a minimum in summer. This is observed at high latitudes over the Atlantic and Pacific (Fig. 2, DJF, 'e') and over the SSTF (Fig. 2, JJA, 'd'). This observation is contrary to previous IASI and MIPAS retrieval results as well, which show seasonal cycles of OCS abundance over oceans which peak in summer [26, 12]. Nevertheless, the overall spatial and seasonal correlations of OCS and CHLA/CDOM abundances observed still support a primary oceanic source in the global OCS distribution.

4.2 Terrestrial biosphere sink

Uptake by the primary vegetative sink is predicted to be correlated with photosynthetic activity. Previous works have identified large tropical forest regions as a significant OCS sink, particularly in the Amazon and Congo Basins [12, 26]. Similar behaviour is expected over the densely forested regions in Southeast Asia[3]. Tropical climates have minimal seasonality, leading to largely constant photosynthetic activity throughout the year. This corroborates well with the results, which show a dominant all-year-round sink feature in these tropical forest regions (Fig. 2, SON, 'f'). Transport of OCS depleted air by prevailing south-easterly winds are observed for these features, which further supports this atmospheric OCS sink. This transport also contributes to OCS depletion at the ITCZ previously observed by Vincent and Dudhia (2017) [26].

[3] See Appendix B

Boreal forests located in high latitudes regions between 50˚–70˚ comprise a significant proportion of the global forest biome[4]. Unlike tropical forests, these regions experience seasonality, with higher photosynthetic activity during boreal summer [36]. The results reveal a widespread reduction in OCS over high latitude land regions during boreal summer (Fig.2, JJA, 'g'), which supports a substantial boreal forest sink.

Overall, both tropical and boreal forests demonstrate spatial and seasonal correlations with the major OCS-depleted features, apart from at very high latitudes. It is noted that tropical OCS depletion is likely increased by OH removal due to higher tropospheric abundances of OH at low latitudes, particularly over tropical forest regions [24]. Nevertheless, the overall observations support a primary vegetative sink for global OCS.

4.3 Diurnal and seasonal variation over land

No observable diurnal variation in global or regional OCS levels is expected. The primary light-dependent ocean sources and vegetative sinks could lead to diurnal variation in regional OCS levels. However, these major sources and sinks are located at the surface, and vertical transport from the surface to the mid-troposphere is slow relative to horizontal advection and diurnal timescales. This would make diurnal variation largely imperceptible to IASI measurements. Possible diurnal variation might arise from oxidation by OH, which is produced via light-dependent reactions. However, OCS removal by OH is slow, and is unlikely to produce noticeable column amount changes on diurnal timescales. As such, the presence of diurnal variation is a likely indicator of anomalous interference, possibly from diurnal surface temperature changes.

Ocean surface temperatures have negligible diurnal variation, which is expected to give fairly constant surface-atmosphere thermal contrast and therefore consistent day and night values over ocean regions. This is the case observed in Fig. 2.

However, significant diurnal variation is persistently present over most land areas as an amplified night time signal, irrespective of high or low daytime OCS levels. This is most clearly observed at land-ocean boundaries, such as at Madagascar and Northern Australia (Fig. 2, MAM, 'h'). These reflect the stark contrast between amplification of the spatially well-defined land features at night and the relatively unchanged ocean features.

Similar to the night time signal amplification, most land signatures are also observed to be stronger in the hemispheric winter than in summer. Clear examples of this are over desert regions during their respective hemispheric winters (Fig. 2, DJF/JJA, 'i').

Both the higher values during night time and winter are possibly due to diurnal land surface temperature (LST) variation. Lower LST gives poorer surface-atmosphere thermal contrast, which could produce greater noise that amplifies the retrieved signal.

However, it is problematic to attribute these variations to LST changes, since poorer thermal contrasts tend to produce a smaller spectral absorption feature. Rather than amplify the signal, these would more likely lead to an underestimation of column amounts. This was the case observed in previous IASI retrievals [26].

Nevertheless, the preliminary conclusion can be made that while other factors might be the primary cause of the high signals, these factors could be compounded by LST changes, leading to the observed diurnal and seasonal variation. Two factors might contribute to this: overcompensation for poor thermal contrasts by the SLR scale-factor, and possible land SSE interference. These are explored further in Section 4.5 and 4.6.

A consistent and highly localised exception to these observations occur in high-altitude regions, such as the Tibetan plateau (Fig. 2, SON, 'j'). Here, slightly higher daytime OCS levels are observed instead.

4.4 Desert region anomalies

Further anomalies are present. In particular, non-tundra desert regions are observed to give consistent and unexpectedly high levels of OCS (Fig. 2, DJF/JJA, 'i'). The retrieved values are higher than even regions of known sources, despite there being no known sources of OCS in desert regions. These features also exhibit sharp spatial edges, and are inconsistent with wind advection. Altogether, these observations suggest that a surface-related effect common to these desert regions might be the cause of the high retrieved values.

4.5 SLR investigations

The SLR is examined to provide insight into these observations. First, the effect of the scale-factor on diurnal variation is explored. Next, the fitting of background signals is evaluated for the anomalously

[4] See Appendix B

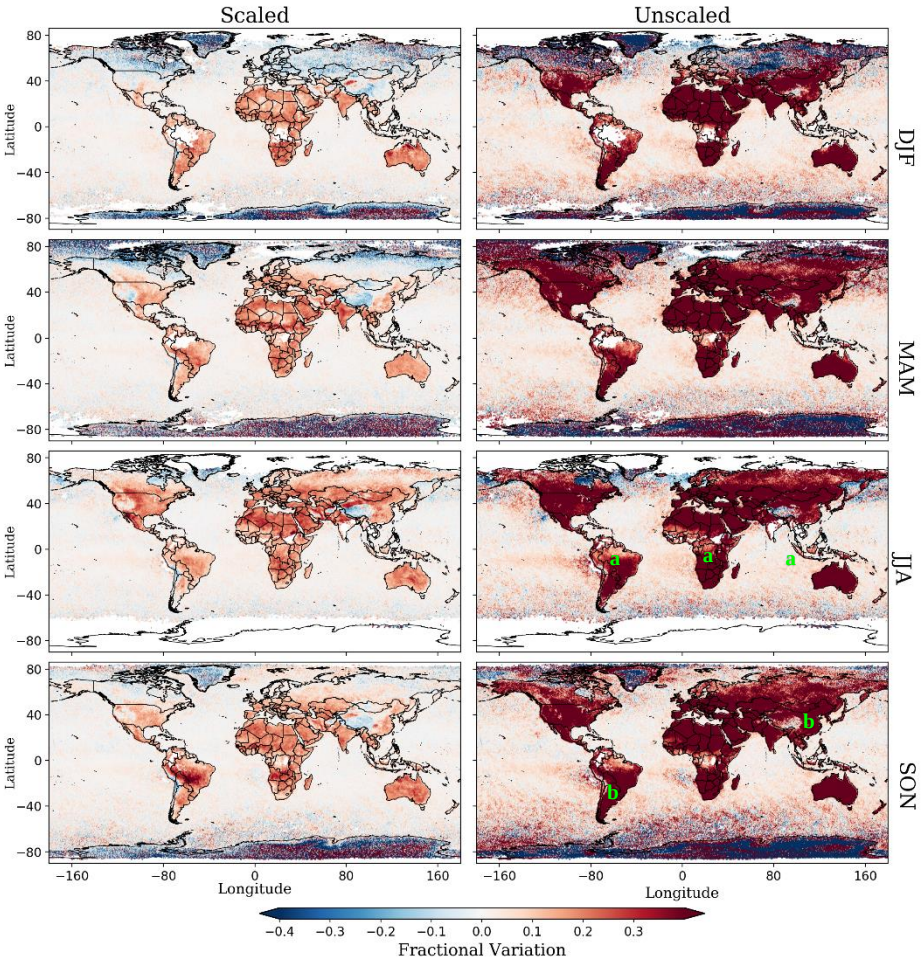

Figure 4: Scaled (left column) and unscaled (right column) distributions of night minus day median values, as a fraction of the global daytime median value, in quarter-yearly intervals of DJF (top row), MAM (second row), JJA (third row) and SON (bottom row), for end 2017 to 2018. Regions without data are shown in white; off-white indicates regions with no diurnal variation.

high values in desert regions. Finally, the ensemble of model atmospheres used in the SLR is evaluated.

4.5.1 Scale-factor

The possible relationship between diurnal variations of LST and retrieved OCS is investigated by evaluating the SLR's response to variable temperature contrasts. As aforementioned, the size of the absorption feature depends not only on OCS amounts but also on the surface-atmosphere thermal contrast. Furthermore, while a typical warm surface and colder OCS-containing atmosphere produces 'absorption' lines, a possibly colder surface under a warmer troposphere would instead produce 'emission' lines. This would be retrieved as a negative column amount. The scale-factor in the SLR therefore attempts to account for the differences in magnitude and sign due to thermal contrast via a multiplicative correction factor, and its efficacy is evaluated here.

Fig. 4 illustrates the impact of the scale-factor on the relative diurnal difference in retrieved values. For bins with both day and night values, the day median is subtracted from the night median, and the difference is presented as a fraction of the global daytime median.

From Fig. 4, it is clear that the unscaled retrieval has a much larger overall fractional diurnal variation. This is observed over most land regions and at very high latitudes, with sharp discontinuities at land-ocean boundaries. The subsequent inclusion of the scale-factor markedly reduces diurnal differences over both land and ocean regions, and greatly improves the land-ocean contrast. This result thus refutes the proposal in Section 4.3 that overcompensation by the scale-factor might be the cause of diurnal and seasonal variation.

A prominent all-year-round feature of low diurnal variation in both scaled and unscaled regimes are the tropical forest regions (Fig. 4, JJA, 'a'). One possible reason is that forested land exhibits dampening of LST variation as compared to non-forested regions [37]. This would further support the idea that LST changes influence diurnal variation in retrieved OCS.

Notably however, high altitude areas also consistently demonstrate minimal diurnal changes in both scaled

and unscaled regimes. This can be observed in the Tibetan Plateau and the South American Andes (Fig. 4, SON, 'b'). Moreover, unlike forested areas, these high altitude regions typically exhibit large diurnal LST variation [38]. As a result, LST is unlikely to be the primary cause of diurnal OCS variation. This validates the initial conclusion from Section 4.3, that LST changes might influence but are unlikely to be the main driving factor of diurnal and seasonal variation.

4.5.2 Background spectral fitting

Next, the high values in desert regions are investigated by evaluating the SLR spectral fitting. In order to isolate the OCS signal, the SLR attempts to fit and remove all background spectral features. This is done by modelling background spectra with spectral patterns derived from the ensemble of atmospheric profiles.

To evaluate the extraction of the OCS signal by the SLR, IASI spectra was fitted only with the background spectral features. This ideally removes all background signals to give a 'residual plot' consisting only of the OCS signature and instrument noise. The residual plot was then fitted with an RFM-generated OCS signal. This was conducted for a spread of locations[5]; plots for the Sahara Desert are shown along with a high-valued region in the Pacific Ocean for comparison (Fig. 5).

From Fig. 5, the residual plots over the Saharan region reveal features that resemble the OCS peaks observed in both the Pacific plots and the fitted RFM-generated signal. This verifies that the SLR measures an OCS-like signal in the high-valued desert regions.

However, background signals are still present, and are notably larger in the Saharan plots. Some background features are also characteristic of other molecular spectra, such as the water vapour peaks at 2020 cm^{-1} and 2060 cm^{-1}, and the CO_2 spike at 2075 cm^{-1} (Fig. 1). These observations indicate imperfect SLR fitting of background absorption. Furthermore, the resulting interference varies in shape and magnitude depending on the scene. The high desert values might thus result from poor fitting of background signals in these regions, which overlap with the OCS peaks and amplify them.

4.5.3 Ensemble of model atmospheres

To provide further insight into fitting of background signals, the ensemble of atmospheres used to account for background absorption was inspected. The profiles

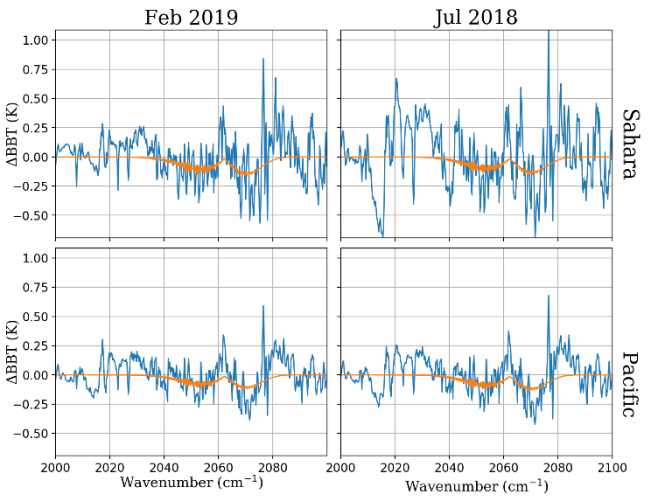

Figure 5: Change in brightness temperature vs wavenumber residual plots (blue) after fitting background features of IASI spectral data from the Sahara Desert (top) and Pacific Ocean (bottom), for the months of February 2019 (left) and July 2018 (right). Residual plots are fitted with the RFM-generated OCS curve (orange). Scaling of axes is the same for all plots.

were generated using meteorological data from a spread of locations, with a further ±10 K surface temperature variation. A map of these locations and the altitude at the base of the atmosphere is shown (Fig. 6).

From Fig. 6, the spread of locations has a wide latitude coverage, and a balanced proportion of both land and water surfaces. However, while the current spread of profiles might be sufficient over oceans, the higher complexity of terrestrial surfaces might require a more representative and extensive ensemble of atmospheres.

Notably, the ensemble lacks profiles in desert regions. It is possible then that significant atmospheric spectral features specific to deserts could have been thus overlooked by the SLR. This might explain the higher background interference observed over the Sahara in the previous section.

Diurnal and seasonal variation in these desert regions might be a further consequence of this lack of profiles.

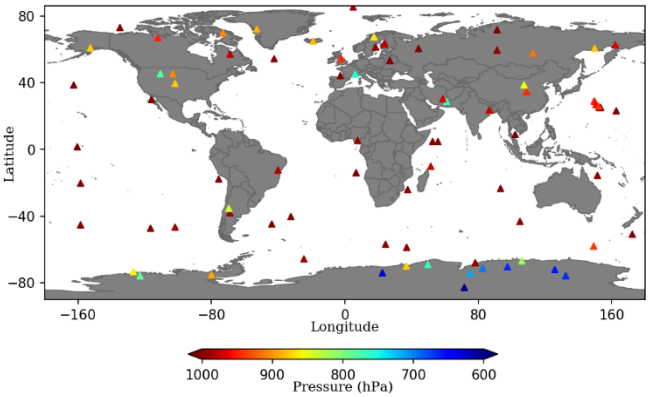

Figure 6: Map of atmospheric profile locations and their respective surface altitudes, given in units of pressure.

[5] See Appendix C

For comparison, high altitude terrain which is well-represented by a spread of atmospheric profiles do not produce such variation.

4.6 Surface spectral emissivity (SSE)

Investigation of the SLR has suggested that surface-related spectral features might be causing the high retrieved values in deserts, and possibly diurnal and seasonal variation. Notably, the SLR does not account for variable SSE, and assumes unitary emissivity (perfect black body) for all surfaces. In Section 3.3, the filters applied to the data only remove possible interference from angular behaviour of SSE. As a result, other spectral features arising from SSE have not been explicitly accounted for by the SLR up to this point.

Two implications are explored in the context of sandy desert regions in the Sahara. The first is possible interference from SSE in background signals. Spectral emissivity of quartz in desert sand was found to affect brightness temperature in the same wavenumber band as the OCS signal[6] [39]. These surface-related features are not generated by the RFM in the atmospheric profiles. As a result, due to poor fitting of these features, overlap of the resultant background signals with OCS peaks might thus enhance retrieved OCS amounts in sandy desert regions.

The second is variable interference due to significant diurnal SSE variation, also observed in sandy deserts. Multiple satellite measurements of sandy regions in the Sahara have shown a consistently larger night time emissivity than in the daytime [40, 41]. This variation occurs within the wavenumber band of interest, and does not vary uniformly with wavenumber[7]. The higher night time emissivity might therefore lead to higher retrieved night values. Overall, both of these examples validate the need for consideration of SSE in the SLR.

4.7 SLR improvements

From the results and discussion, some improvements to the SLR are proposed. First, the present ensemble of atmospheric profiles should be expanded to include currently underrepresented regions. Specifically, the addition of profiles from deserts might improve retrievals over these regions, and help resolve the anomalously high retrieved values.

Secondly, spectral patterns arising from SSE and from diurnal SSE variation for different surface types could be incorporated into the SLR. Atmospheric profiles do not capture surface-related effects, and so spectral emissivity features from typical surface types (e.g. quartz) could be added to the main spectral components for the retrieval. In addition to this, a range of emissivity values could be programmed into the RFM when modelling the atmospheric profiles.

5. CONCLUSION

The new experimental SLR algorithm was applied to IASI data to retrieve global OCS column amounts over a year. Overall, global seasonal distributions showed significant features which support previous results and literature on the primary oceanic source and terrestrial vegetative sink [6, 9, 26, 12].

Unexpected diurnal and seasonal OCS variations were observed over land surfaces, with consistently higher retrieved values during night time and in winter. The stark land-ocean contrasts of these features suggest that these variations might be due to interference from land surface effects. Desert regions also displayed anomalously high OCS levels, in the absence of known sources. The sharp spatial edges of these features similarly suggest region-specific surface effects.

These observations led to investigation of the SLR algorithm in a few ways. First, the impact of scaling was assessed. The results showed that inclusion of the scale-factor improved fractional diurnal OCS variation in all regions, and substantially so over land areas. Next, evaluation of background absorption fitting by the SLR revealed larger interference from background spectral features over the Sahara Desert than in other regions. This is possibly due to the lack of desert profiles found on examination of the ensemble of atmospheres.

Notably, the current SLR algorithm makes no consideration of variable spectral emissivity. The effect of quartz emissivity in sandy desert regions is thus the likely primary cause of the anomalously high values in deserts. Furthermore, diurnal SSE variation produces higher desert emissivity at night. This could be a crucial factor leading to the higher night time OCS values.

Improvements to the SLR were therefore suggested. The spread of atmospheric profiles used could be expanded to include a wider variety of terrain. This would hopefully improve fitting of background absorption in currently underrepresented regions. In addition to this, variable SSE and diurnal SSE variation

[6] See Appendix D

[7] See Appendix E

could be incorporated into the retrieval. This could be done by including SSE spectral patterns from typical surface types into the main spectral components of the retrieval. Additionally, a range of emissivity values could be considered in the RFM when generating the atmospheric profiles from meteorological data.

Refinements to the SLR to rectify these anomalies would be necessary before feasible quantitative estimates of global production and consumption of OCS can be made. In particular, the large variation due to the anomalies in the present data could have obscured the impact of secondary sources and sinks. A notable example is the anthropogenic source that was predicted and previously observed in Eastern China [1, 26, 13]. These features were not observed in the OCS distributions obtained, possibly due to high-valued anomalies interfering in these regions or skewing the scale. Improving the efficacy of the SLR would provide further insight into these secondary effects, and could also shed light on less well-researched phenomena, such as the postulated precipitation source.

6. REFERENCES

[1] C. Brühl et al., 2012, doi:10.5194/acp-12-1239-2012.
[2] M. P. Barkley et al., 2008, doi:10.1029/2008GL034270.
[3] S. A. Montzka et al., 2007, doi:10.1029/2006JD007665.
[4] T. S. Bates et al., 1992, doi:10.1007/BF00115242.
[5] T. Miyakawa et al., 2007, doi:10.1029/2006JD007896.
[6] M. E. Whelan et al., 2018, doi:10.5194/bg-15-3625-2018.
[7] A. J. Kettle et al., 2002, doi:10.1029/2002JD002187.
[8] J. X. Sheng et al,, 2014, doi:10.1002/2014JD021985.
[9] J. Berry et al., 2013, doi:10.1002/jgrg.20068.
[10] A. Dudhia, 2020. [Online] http://eodg.atm.ox.ac.uk/user/dudhia/iasi/reports/slr.pdf.
[11] J. E. Campbell et al., 2015. doi:10.1002/2015GL063445.
[12] N. Glatthor et al., 2015, doi:10.1002/2015GL066293.
[13] A. Zumkehr et al., 2018, doi:10.1016/j.atmosenv.2018.03.063.
[14] S. Lennartz et al., 2017, doi:10.5194/acp-17-385-2017.
[15] M. D. Keller, 1989, doi:10.1080/01965581.1988.10749540.
[16] I. Barnes et al., 1996, doi:10.1016/1352-2310(95)00389-4.
[17] T. Berndt et al., 2019, doi:10.1021/acs.jpclett.9b02567.
[18] K. Mopper & D. J. Kieber, "Chapter 9 – Photochemistry and the Cycling of Carbon, Sulfur, Nitrogen and Phosphorus," in *Biogeochemistry of Marine Dissolved Organic Matter*, Academic Press, 2002, pp. 455-507.
[19] J. R. Stinecipher et al., 2019, doi:10.1029/2019GL085567.
[20] Y. Mu et al., 2004, doi:10.1029/2003JD004206.
[21] C. Textor et al., 2003, https://www.academia.edu/28112633/Emissions_from_volcanoes
[22] R. Commane et al., 2015, doi:10.1073/pnas.1504131112.
[23] L. M. J. Kooijmans et al., 2017, doi:10.5194/acp-17-11453-2017.
[24] J. Lelieveld et al., 2016, doi:10.5194/acp-16-12477-2016.
[25] L. Kuai et al., 2015, doi:10.1002/2015JD023493.
[26] R. A. Vincent & A. Dudhia, 2017, doi:10.5194/acp-17-2981-2017.
[27] World Metereological Organization, 2020. [Online]. https://www.wmo-sat.info/oscar/instruments/view/207.
[28] A. Dudhia, 2017, doi:10.1016/j.jqsrt.2016.06.018.
[29] V. García-Santos et al., 2012, doi:10.1029/2012JD017931.
[30] J. A. Hanafin & P. J. Minnett, 2005, doi:10.1364/AO.44.000398.
[31] J. N. Boyer et al., 2009, doi:10.1016/j.ecolind.2008.11.013.
[32] D. Aurin et al., 2018, doi:10.3390/app8122687.
[33] D. G. Capone & D. A. Hutchins, 2013, doi:10.1038/ngeo1916.
[34] N. Ramaiah et al., 2015, doi:10.1016/j.dsr2.2015.03.013.
[35] S. Wang et al., 2018, doi:10.1007/s10533-018-0430-5.
[36] Q. Yang et al., 2020, doi:10.1038/s41467-019-13954-0.
[37] R. Alkama & A. Cescatti, 2016, doi:10.1126/science.aac8083.
[38] Y. Oku & H. Ishikawa, 2004, https://www.jstor.org/stable/26185933
[39] D. K. Zhou et al., 2011, doi:10.1109/TGRS.2010.2051036.
[40] G. Masiello et al., 2013, doi:10.1002/jgrd.50863.
[41] Z. Li et al., 2012, doi:10.1029/2012JD018279.

7. APPENDICES

List of Appendices:

A. Bibliography
B. Map of forested regions
C. Residual plots from other locations
D. Quartz infrared emissivity
E. Diurnal variation of quartz emissivity

Appendix A: Bibliography

[1] C. Brühl et al., "The role of carbonyl sulphide as a source of stratospheric sulphate aerosol and its impact on climate," *Atmos. Chem. Phys.*, vol. 12, no. 3, pp. 1239-1253, 2012.

[2] M. P. Barkley et al., "Global distributions of carbonyl sulfide in the upper troposphere and stratosphere," *Geophys. Res. Lett.*, vol. 35, no. 14, 2008.

[3] S. A. Montzka et al., "On the global distribution, seasonality, and budget of atmospheric carbonyl sulfide (COS) and some similarities to CO2," *J. Geophys. Res.*, vol. 112, no. D09302, 2007.

[4] T. S. Bates et al., "Sulfur Emissions to the Atmosphere from Natural Sources," *J. Atmos. Chem.*, vol. 14, no. 1-4, pp. 315-337, 1992.

[5] T. Miyakawa et al., "Removal of sulfur dioxide and formation of sulfate aerosol in Tokyo," *J. Geophys. Res. Atmos.*, vol. 112, no. D13209, 2007.

[6] M. E. Whelan et al., "Reviews and syntheses: Carbonyl sulfide as a multi-scale tracer for carbon and water cycles," *Biogeosciences*, vol. 15, no. 12, p. 3625–3657, 2018.

[7] A. J. Kettle et al., "Global budget of atmospheric carbonyl sulfide: Temporal and spatial variations of the dominant sources and sinks," *J. Geophys. Res.*, vol. 107, no. D22, p. 4658, 2002.

[8] J. X. Sheng et al,, "Global atmospheric sulfur budget under volcanically quiescent conditions: Aerosol-chemistry-climate model predictions and validation," *J. Geophys. Res. Atmos.*, vol. 120, no. 1, p. 256–276, 2014.

[9] J. Berry et al., "A coupled model of the global cycles of carbonyl sulfide and CO2: A possible new window on the carbon cycle," *J. Geophys. Res. Biogeosci.*, vol. 118, no. 2, p. 842–852, 2013.

[10] A. Dudhia, "Scaled Linear Retrieval," 12 March 2020. [Online] http://eodg.atm.ox.ac.uk/user/dudhia/iasi/reports/slr.pdf. [Accessed 23 03 2020].

[11] J. E. Campbell et al., "Atmospheric carbonyl sulfide sources from anthropogenic activity: Implications for carbon cycle constraints," *Geophys. Res. Lett.*, vol. 42, no. 8, pp. 3004-3010, 2015.

[12] N. Glatthor et al., "Tropical sources and sinks of carbonyl sulfide observed from space," *Geophys. Res. Lett.*, vol. 42, pp. 10,082–10,090, 2015.

[13] A. Zumkehr et al., "Global gridded anthropogenic emissions inventory of carbonyl sulfide," *Atmos. Environ.*, vol. 183, pp. 11-19, 2018.

[14] S. Lennartz et al., "Direct oceanic emissions unlikely to account for the missing source of atmospheric carbonyl sulfide," *Atmos. Chem. Phys.*, vol. 17, pp. 385-402, 2017.

[15] M. D. Keller, "Dimethyl Sulfide Production and Marine Phytoplankton: The Importance of Species Composition and Cell Size," *Biological Oceanography*, vol. 6, no. 5-6, pp. 375-382, 1989.

[16] I. Barnes et al., "FTIR product study of the OH initiated oxidation of dimethyl sulphide: Observation of carbonyl sulphide and dimethyl sulphoxide," *Atmos. Environ.*, vol. 30, pp. 1805-1814, 1996.

[17] T. Berndt et al., "Fast Peroxy Radical Isomerization and OH Recycling in the Reaction of OH Radicals with Dimethyl Sulfide," *J. Phys. Chem. Lett.*, vol. 10, no. 21, pp. 6478-6483, 2019.

[18] K. Mopper & D. J. Kieber, "Chapter 9 – Photochemistry and the Cycling of Carbon, Sulfur, Nitrogen and Phosphorus," in *Biogeochemistry of Marine Dissolved Organic Matter*, Academic Press, 2002, pp. 455-507.

[19] J. R. Stinecipher et al., "Biomass Burning Unlikely to Account for Missing Source of Carbonyl Sulfide," *Geophys. Res. Lett.*, vol. 46, no. 24, pp. 14912-14920, 2019.

[20] Y. Mu et al., "Photochemical production of carbonyl sulfide in precipitation," *J. Geophys. Res. Atmos.*, vol. 109, no. D13, 2004.

[21] C. Textor et al., "7 Emissions from Volcanoes," in *Emissions of Chemical Compounds and Aerosols in the Atmosphere*, Dordrecht, Kluwer Academic Publishers, 2003.

[22] R. Commane et al., "Seasonal fluxes of carbonyl sulfide in a midlatitude forest," *PNAS*, vol. 112, no. 46, p. 14162–14167, 2015.

[23] L. M. J. Kooijmans et al., "Canopy uptake dominates nighttime carbonyl sulfide fluxes in a boreal forest," *Atmos. Chem. Phys.*, vol. 17, no. 18, pp. 11453-11465, 2017.
[24] J. Lelieveld et al., "Global tropospheric hydroxyl distribution, budget and reactivity," *Atmos. Chem. Phys.*, vol. 16, pp. 12477-12493, 2016.
[25] L. Kuai et al., "Estimate of carbonyl sulfide tropical oceanic surface fluxes using Aura Tropospheric Emission Spectrometer observations," *J. Geophys. Res. Atmos.*, vol. 120, no. 20, pp. 11,012-11,023, 2015.
[26] R. A. Vincent & A. Dudhia, "Fast retrievals of tropospheric carbonyl sulfide with IASI," *Atmos. Chem. Phys.*, vol. 17, no. 4, pp. 2981-3000, 2017.
[27] World Metereological Organization, "OSCAR - Instrument: IASI," 2020. [Online]. https://www.wmo-sat.info/oscar/instruments/view/207. [Accessed 14 04 2020].
[28] A. Dudhia, "The Reference Forward Model (RFM)," *J. Quant. Spectrosc. Radiat. Transfer*, vol. 186, pp. 243-253, 2017.
[29] V. García-Santos et al., "On the angular variation of thermal infrared emissivity of inorganic soils," *J. Geophys. Res.*, vol. 117, no. D19116, 2012.
[30] J. A. Hanafin & P. J. Minnett, "Measurements of the infrared emissivity of a wind-roughened sea surface," *Appl. Opt.*, vol. 44, no. 3, pp. 398-411, 2005.
[31] J. N. Boyer et al., "Phytoplankton bloom status: Chlorophyll a biomass as an indicator of water quality condition in the southern estuaries of Florida, USA," *Ecol. Indic.*, vol. 9, no. 6, pp. S56-S67, 2009.
[32] D. Aurin et al., "Remote Sensing of CDOM, CDOM Spectral Slope, and Dissolved Organic Carbon in the Global Ocean," *Appl. Sci.*, vol. 8, no. 12, p. 2687, 2018.
[33] D. G. Capone et al., "Microbial biogeochemistry of coastal upwelling regimes in a changing ocean," *Nat. Geosci.*, vol. 6, p. 711–717, 2013.
[34] N. Ramaiah et al., "Response of bacteria and phytoplankton from a subtropical front location Southern Ocean to micronutrient amendments ex-situ," *Deep Sea Res. Part II*, vol. 118, no. Part B, pp. 209-220, 2015.
[35] S. Wang et al., "Influence of dimethyl sulfide on the carbon cycle and biological production," *Biogeochemistry*, vol. 138, pp. 49-68, 2018.
[36] Q. Yang et al., "Two dominant boreal conifers use contrasting mechanisms to reactivate photosynthesis in the spring," *Nat. Commun.*, vol. 11, p. 128, 2020.
[37] R. Alkama & A. Cescatti, "Biophysical climate impacts of recent changes in global forest cover," *Science*, vol. 351, no. 6273, pp. 600-604, 2016.
[38] Y. Oku & H. Ishikawa, "Estimation of land surface temperature over the Tibetan Plateau using GMS data," *J. Appl. Meteor.*, vol. 43, pp. 548–561, 2004.
[39] D. K. Zhou et al., "Global land surface emissivity retrieved from satellite ultraspectral ir measurements", *IEEE Trans. Geosci. Remote Sens.*, vol 49, no. 4, pp. 1277-1290, 2011.
[40] G. Masiello et al., "Diurnal variation in Sahara desert sand emissivity during the dry season from IASI observations," *J. Geophys. Res. Atmos.*, vol. 119, no. 3, pp. 1626-1638, 2013.
[41] Z. Li et al., "Determining diurnal variations of land surface emissivity from geostationary satellites," *J. Geophys. Res. Atmos.*, vol. 117, no. D23, 2012.
[42] M.A.K. Khalil, et al., "Global sources, lifetimes and mass balances of carbonyl sulfide (OCS) and carbon disulfide (CS2) in the earth's atmosphere," *Atmospheric Environment (1967)*, vol. 18, no. 9, pp. 1805-1813, 1984.
[43] S. F. Watts, "The mass budgets of carbonyl sulfide, dimethyl sulfide, carbon disulfide and hydrogen sulfide," *Atmospheric Environment*, vol. 34, no. 5, pp. 761-779, 2000.
[44] S. Blezinger et al., "Enzymatic consumption of carbonyl sulfide (COS) by marine algae," *Biogeochemistry*, vol. 48, no. 2, pp. 185-197, 2000.
[45] S. Kremser et al., "Positive trends in Southern Hemisphere carbonyl sulfide," *Geophys. Res. Lett.*, vol. 42, pp. 9473–9480, 2015.
[46] G. C. Toon & J. L. Blavier & K. Sung, "Atmospheric carbonyl sulfide (OCS) measured remotely by FTIR solar absorption spectrometry", *Atmos. Chem. Phys.*, vol. 18, pp. 1923–1944, 2018.
[47] N. J. Blake et al., "Carbonyl sulfide and carbon disulfide: Large-scale distributions over the western Pacific and emissions from Asia during TRACE-P", *J. Geophys. Res.*, vol. 109, no. D15, 2004.
[48] F. Hilton et al., "Hyperspectral Earth Observation from IASI: Five Years of Accomplishments", *Bull. Am. Meteorol. Soc.*, vol. 93, no. 3, pp. 347-370, 2012.
[49] C.Camy-Peyret et al., "Assessment of IASI capability for retrieving carbonyl sulphide (OCS)", *J. Quant. Spectrosc. RA.*, vol. 201, pp. 197-208, 2017.

Appendix B: Map of Forested Regions by Domain (© FAO (2010) "World's Forest 2010 by Climatic Domain" Retrieved from http://www.fao.org/forestry/fra/80298/en/ on 25/03/2020)

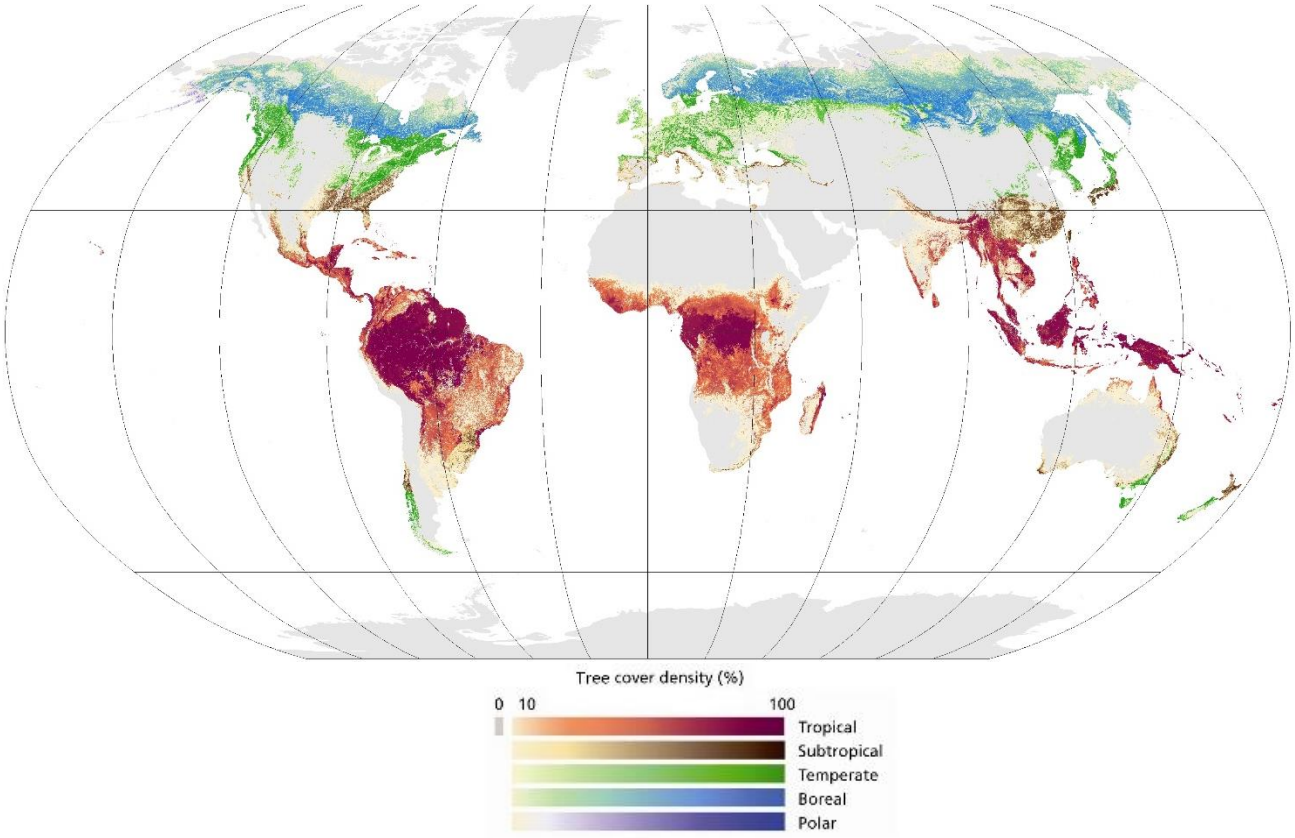

Appendix C: Residual plots for other regions, with table of fitted ratios, using RFM generated OCS signal. Locations are in high latitude regions (Antarctica, Arctic ocean, Greenland), ocean regions (Atlantic (low-level region), Pacific (high-level region)), and desert regions (Australia, Gobi, North America, Sahara)

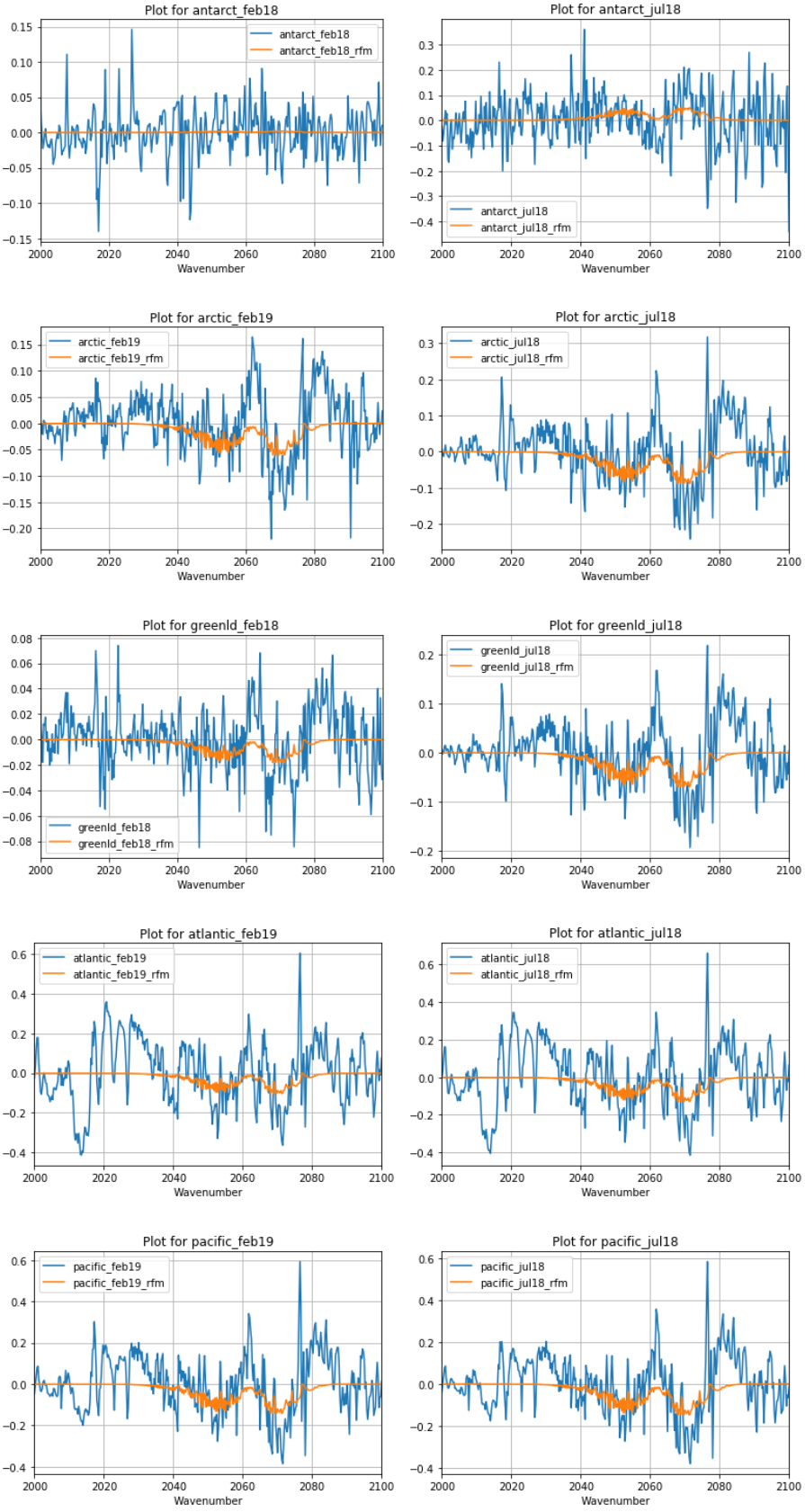

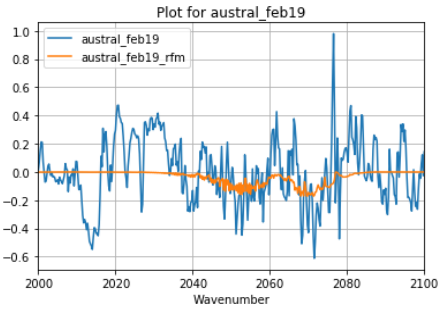
Plot for austral_feb19
austral_feb19
austral_feb19_rfm
Wavenumber

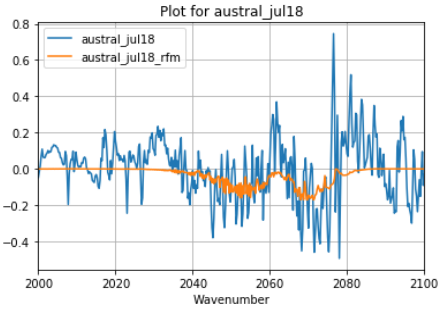
Plot for austral_jul18
austral_jul18
austral_jul18_rfm
Wavenumber

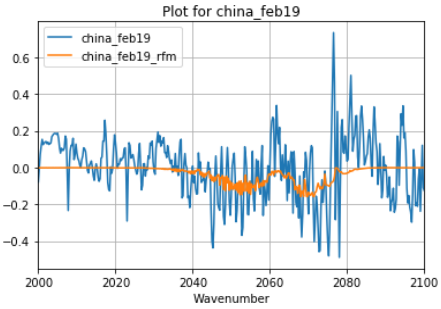
Plot for china_feb19
china_feb19
china_feb19_rfm
Wavenumber

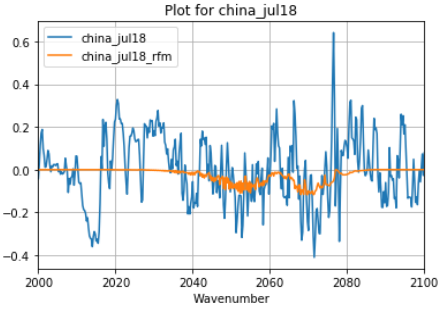
Plot for china_jul18
china_jul18
china_jul18_rfm
Wavenumber

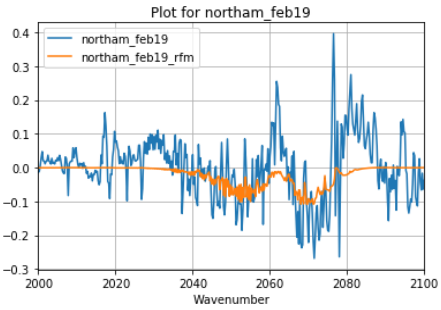
Plot for northam_feb19
northam_feb19
northam_feb19_rfm
Wavenumber

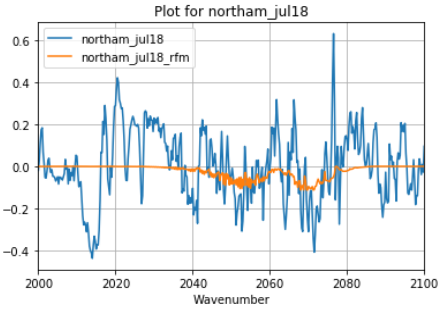
Plot for northam_jul18
northam_jul18
northam_jul18_rfm
Wavenumber

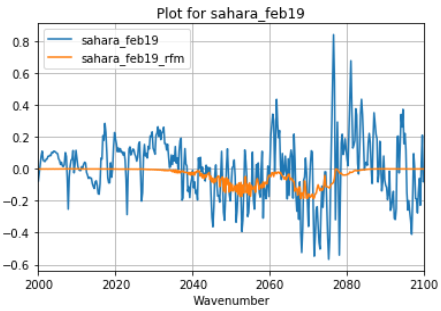
Plot for sahara_feb19
sahara_feb19
sahara_feb19_rfm
Wavenumber

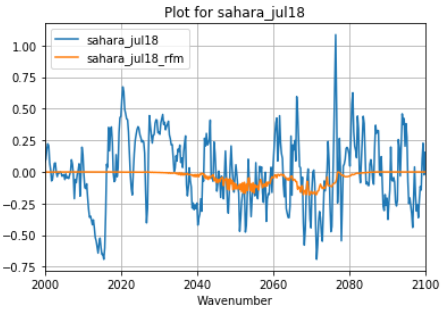
Plot for sahara_jul18
sahara_jul18
sahara_jul18_rfm
Wavenumber

Appendix D: (b) In green, the retrieved change in brightness temperature due to surface emissivity, (c) Retrieved surface spectral emissivity over the Sahara Desert during daytime (D. K. Zhou et al., "Global Land Surface Emissivity Retrieved From Satellite Ultraspectral IR Measurements", *IEEE Transactions on Geoscience and Remote Sensing*, vol 49, no. 4, pp. 1277-1290, 2011.) (Added) Highlighted region indicates wavenumber window of interest.

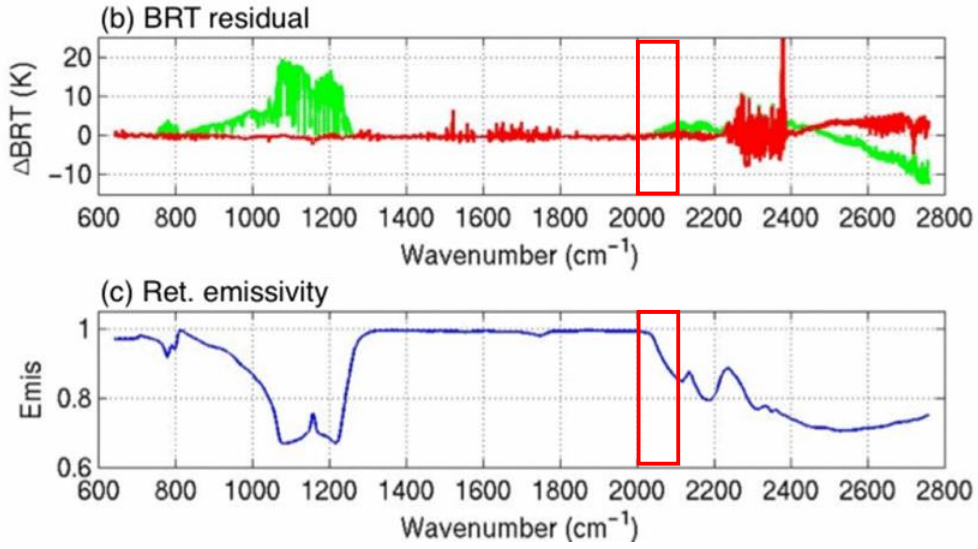

Appendix E: Day and night average emissivity computed on the basis of the 28 pairs of IASI soundings for 6 July 2010 [in sand dune Saharan regions, cloudless, no rain]. (a) Daytime average emissivity; (b) night time average emissivity. The figure also shows the average emissivity obtained by the UW/BFEMIS database. (G. Masiello, et al., "Diurnal variation in Sahara desert sand emissivity during the dry season from IASI observations," *J. Geophys. Res. Atmos.*, vol. 119, no. 3, pp. 1626-1638, 2013.). (Added, in green) Note the diurnal variation in emissivity observed in the wavenumber region of interest (2000 cm^{-1} to 2100 cm^{-1}).